HHS Public Access

Author manuscript

*Acad Radiol*. Author manuscript; available in PMC 2019 November 01.

Published in final edited form as:

*Acad Radiol*. 2018 November ; 25(11): 1405–1414. doi:10.1016/j.acra.2018.02.010.

# Multiparametric Whole-Body MRI with Diffusion-Weighted Imaging and ADC Mapping for the Identification of Visceral and Osseous Metastases from Solid Tumors

**Michael. A. Jacobs**[1,2], **Katarzyna J. Macura**[1,2], **Atif Zaheer**[1], **Emmanuel S. Antonarakis**[2], **Vered Stearns**[2], **Antonio C. Wolff**[2], **Thorsten Feiweier**[4], **Ihab R. Kamel**[1], **Richard L. Wahl**[1,2,3], and **Li Pan**[5]

[1]The Russell H. Morgan Department of Radiology and Radiological Science, The Johns Hopkins University School of Medicine, Baltimore, MD 21205

[2]Sidney Kimmel Comprehensive Cancer Center, The Johns Hopkins University School of Medicine, Baltimore, MD 21205

[3]Mallinckrodt Institute of Radiology, Washington University St. Louis, MO 63130

[4]Siemens Healthcare GmbH, Erlangen, Germany, 91052

[5]Siemens Healthcare, Baltimore, MD, 21287

## Abstract

**Rationale and Objectives—**The purpose of this study was to investigate the use of multiparametric, whole-body, diffusion-weighted imaging (WB-DWI) and Apparent Diffusion Coefficient (ADC) maps with $T_2$-weighted MRI at 3T for the detection and monitoring of metastatic disease in patients.

**Materials and Methods—**Fifty-four participants (32 healthy subjects and 22 patients) were scanned with WB-DWI methods using a 3T MRI scanner. Axial, sagittal, or coronal fat-suppressed $T_2$-weighted ($T_2$WI), $T_1$-weighted($T_1$WI), and DWI images were acquired. Total MRI acquisition and set up time was approximately 45 minutes. Metastatic disease on MRI was confirmed based on $T_2$WI characteristics. The number of lesions were established on Computed Tomography (CT) or PET/CT. Whole-body ADC maps and $T_2$WI were constructed and region-of-interests (ROIs) were drawn in normal and abnormal-appearing tissue for quantitative analysis. Statistical analysis was performed using a paired t-tests and $p<0.05$ was considered statistically significant.

**Results—**There were 91 metastatic lesions detected from the CT or PET/CT with a missed recurrent lesion in the prostate. Multiparametric WB-MRI had excellent sensitivity (96%) for detection of metastatic lesions compared to CT. ADC map values and the ADC ratio in metastatic

Address Correspondence To: Michael A. Jacobs, Ph.D., Department of Radiology, The Johns Hopkins University School of Medicine, Traylor Bldg., Rm 309, 712 Rutland Ave, Baltimore, MD 21205, Tel:410-955-7483, Fax:410-614-1948, mikej@mri.jhu.edu.

bone lesions were significantly increased ($p<0.05$) compared to normal bone. In soft tissue, ADC map values and ratios in metastatic lesions were decreased compared to normal soft tissue.

**Conclusion—**We have demonstrated that multiparametric WB-MRI is feasible for oncologic staging to identify bony and visceral metastasis in breast, prostate, pancreatic, and colorectal cancers. WB-MRI can be tailored to fit the patient, such that an "individualized patient sequence" can be developed for a comprehensive evaluation for staging and response during treatment.

### Keywords

Metastatic disease; whole-body magnetic resonance imaging; magnetic resonance imaging; diffusion-weighted imaging; breast; prostate; colon; cancer

## Introduction

Metastatic disease and/or local recurrences of cancer have an unfavorable prognosis. Treatment approaches for distant metastases are mostly palliative rather than curative. Skeletal or organ metastasis is usually not detected until clinical symptoms appear, or during initial staging of cancer by imaging (1,2). If metastatic disease is found, most patients will receive various systemic therapy regimens, with the goal of ameliorating symptoms and improving survival. Although Positron Emission Tomography/Computed Tomography (PET/CT) covers most of the body, measures the metabolic activity of a tumor and is used for staging and treatment response, PET maybe limited by other factors, such as high uptake in normal organs, variability in tracer uptake in lesions, increased radiation dose or indeterminate findings due to the size of the lesion (less than 1cm)(3,4). Therefore, there is a need for an imaging method that achieves global tumor assessment and accurate lesion detection for increased confidence in the detection, characterization, and monitoring of treatment response in metastatic disease without an increase in radiation dose.

To address these challenges, developments in whole-body MRI (WB-MRI) technology have resulted in whole-body coverage using anatomical $T_1$- or $T_2$-weighted imaging at 1.5T (5–10). Some of the improvements are specialized surface coils, continuous table movement (CTM), improved respiratory gating, planning software and pulse sequences. These system improvements in MRI technology have led to impressive results in both oncological and non-oncological applications of WB-MRI compared to more conventional imaging methods(4,11–14). As it turns out, most of the applications have been limited to anatomical and qualitative MRI parameters. There is a growing need to accurately quantify functional properties of the tissue, since these metrics represent early biological changes before anatomical MRI parameters. In particular, advanced quantitative MRI parameters such as diffusion-weighted imaging (DWI) with Apparent Diffusion Coefficient (ADC) maps, and dynamic contrast-enhanced (DCE)-MRI can provide metrics of the molecular and vascular characteristics of tumors (15–18). There are several reports in the literature about the feasibility of using WB-DWI in different cancers (19–24). However, only a few of these WB-DWI methods have been applied to whole-body imaging at 3T (25–27). Therefore, we have implemented multiparametric WB-MRI, coupled with DWI and quantitative ADC mapping at 3T, to provide functional and quantitative information about normal and tumor (primary or metastatic) tissue and compare the WB-MRI results to patients that received CT

or PET/CT. This development of quantitative DWI WB-MRI provides the opportunity to investigate the detection and characterization of metastatic areas in the body without the need for ionizing radiation.

## Materials and Methods

### Clinical Subjects

Volunteers (n=32; age range:27–65 years old) and patients (n=22; age range:39–80 years old) who were scheduled for conventional imaging were enrolled in this *prospective* study. Patients were selected for the study based on the potential for metastases or had metastatic disease identified by a referring oncologist. This study was approved by the IRB at our facility and conforms to HIPAA requirements.

### Metastatic Lesion Classification

Two board-certified radiologists defined suspicious metastatic lesions based on computed tomography (CT) and if available, a nuclear-based imaging (Tc99m or PET) and the WB-MRI. Lesions were identified using radiological characteristics of metastasis, such as the Bulls-Eye sign (where there is increased signal intensity within the center of a suspected region), Halo sign (characterized by an increased signal intensity around the periphery of a suspected region), and/or increased/decreased signal intensity on anatomical images (28,29). Incidental lesions were not included in the total number of lesions in this study.

### MRI Imaging

**WB-MRI Protocol—**All studies were performed on a dedicated clinical research 3T scanner (MAGNETOM Trio, a Tim System, Siemens Healthcare, Erlangen, Germany) using the Total Imaging Matrix (Tim) with Continuous Table Movement (CTM). This technology enables the application of multiple phased-array surface coils and receiver channels for parallel imaging in three spatial directions while acquiring sections of the body from head down to mid-tibia. The total scan range of 205cm can be obtained by combining the large field-of-view (FOV) between 400–500 mm with automatic table movement. For the axial plane, four to nine stations were scanned, or CTM was performed; and, in the coronal and/or sagittal planes, four to six stations were acquired ranging from head to mid-tibia. A depiction of a multiparametric WB-MRI in a normal subject with representative anatomical sections that can be acquired and composed is shown Figure 1.

**Proton MR Imaging—**Whole-body axial, coronal, or sagittal images were obtained, consisting of fat-suppressed Short Tau Inversion Recovery (STIR) $T_2$-weighted images (TR/TE=6640/84ms, FOV=400–500×400–500mm$^2$, matrix=400×400, slice thickness(ST)=4–6mm). A $T_1$-weighted (TR/TE=4340ms/53ms, FOV=400–500×400–500mm$^2$, matrix=400×400, inversion time (TI)=220ms, ST=1.5–6mm) protocol with a 2D PACE (Prospective Acquisition CorrEction) technique was used in the thorax and abdomen regions to reduce motion artifacts. Typical voxel sizes were 1.25–0.9 mm, depending on body habitus. Total time for this portion of the WB-MRI was 30–35 minutes

**Quantitative Diffusion-Weighted Imaging and Apparent Diffusion Coefficient Mapping—**DWI with multiple b-values was obtained using a fat-suppressed spin echo EPI prototype sequence (FOV=400–500×400–500mm$^2$, Matrix=192×192 TR/TE = 5600–7500ms/60–75ms, TI=240ms, b=50, 400 and 800s/mm$^2$, averages=4, ST=5mm, bandwidth= 2706 Hz/pixel, echo spacing=0.45ms, acceleration factor=2). Typical voxel sizes were 2.6–1.9 mm, depending on body habitus. The acquisition of different b-values allows for the creation of trace ADC maps on a pixel-by-pixel basis for quantitative analysis. Monoexponential ADC maps were created for the WB-MRI using the scanner software. Total acquisition time (axial, coronal, or sagittal) for DWI was approximately 15–20 minutes. Total Time from set up to finish is 45–60 minutes depending on the size of the patient.

**2D PACE Respiratory Gating—**The 2D PACE (Prospective Acquisition CorrEction) technique is incorporated into WB-MRI sequences to decrease respiratory/organ motion and other artifacts. Prior to the MRI measurement, 2D PACE acquires fast gradient echo images during free breathing, in which, the user determines an acceptance window (typically 2cm) based on the vertical width of a region of interest that is placed at the dome of the liver. 2D PACE measures the displacement of the diaphragm during breathing and after a short "learning phase," the patient's breathing pattern is analyzed and the central position of an "acceptance window" is automatically calculated. The real-time evaluation of the navigator signal allows for the immediate start of the MRI data acquisition as soon as the diaphragm has reached a position within the acceptance window. The navigator image was acquired within 100ms with a low-resolution gradient echo sequence using a low flip angle. This prolongs the measurement time, with a resulting TR of about 3 to 4s (breathing cycle).

## Computed Tomography and Positron Emission Tomography

Computed tomography, with and without contrast, was acquired using standard clinical protocols (120 kilovolt peak (KVp), 100–275 milliAmp-sec(mAs), 0.5–0.75 seconds rotation time, 512×512 matrix) to examine the chest, thorax, abdomen, and pelvis. The contrast used was Omnipaque from 100cc to 150cc depending on patient weight and injected intravenously at a rate of 2 to 5 mL per second. The typical window/level (W/L) ranges used to visual tissue for CT were as follows: lung, W/L = −500 to −600/1500–1600, Bone, W/L =2000–2500/300–480, Soft tissue; W/L =350–400/40–50. Windowing of the tissue was tailored by the radiologist for each patient.

PET/CT data was acquired using a Discovery Light Speed (General Electric, Milwaukee, Wisconsin) scanner on patients after they had fasted for four hours. $^{18}$F-fluorodeoxyglucose ($^{18}$FDG) or $^{11}$C choline acetate was injected into the patient. The radionuclide dose is calculated based on the weight (kg) of the patient, as follows: Dose (mCi) = Weight (kg) * 0.22(mCi/kg. Maximum dose is 25mCi for weights greater than 114kg or 250lbs. Minimum dose is 5mCi for weights less than 23kg or 51lbs. After the uptake phase, which lasts 45–60 minutes, the patient is positioned and near-whole-body images are acquired using a PET/CT unit, which enables the calculation of the standardized uptake value (SUV) (30).

### Radiological Image Preprocessing and Analysis

**Normal and Lesion Tissue Analysis—**Whole-body images of $T_2$WI, DWI, and ADC maps from patients were reconstructed using an in-line processing "Composer" tool on the syngo workstation. The WB-MRI and PET/CT were divided into standard anatomical sections consisting of the head, neck, chest, abdomen, pelvis, and lower extremities. The number of suspected lesions within each region were counted from each modality. Regions of interest (ROI) were drawn on normal and lesion tissue. For lesion tissue, both b value images at zero and 400s/mm$^2$ were used to label the ROI for quantitative analysis on the ADC map (See Figures 2 and 3). ADC map values and mean ± standard deviation (SD) were calculated and recorded. Normal tissue ADC map values were selected from different regions in the brain, thorax, chest (breast), abdomen (liver, gallbladder, kidney, spleen), pelvis (prostate or uterus), and lower extremities in all subjects. In the normal tissue, ROIs were drawn to encompass most of the tissue. For lesion tissue, a region growing method was used for each ROI and morphological operations were used to ensure that ROI was contained within the lesion. Similar ROI analysis was performed on the PET/CT to calculate the SUV in areas of liver and lesion tissue. For PET ROI analysis, lesion tissue was selected based on the elevation of the SUV from normal SUV uptake within the liver(31). Ratios were calculated between the lesion-to-normal tissue or normal-to-normal tissue (e.g., right vs. left) for the ADC map values according to the modified equation below (18).

$$\text{Normalized ADC value} = \frac{\text{ADC value of lesion}}{\text{ADC value of normal tissue}}$$

This ratio metric enables comparison of different tissue values across subjects.

### Statistical Analysis

Summary statistics (mean and standard deviations) from the quantitative imaging parameters were determined for the subjects. The differences between ADC map values of normal and lesion tissue were tested between controls and patients using unpaired t-tests. Statistical significance was set at $p<0.05$.

## RESULTS

### Clinical Characteristics

Normal volunteers (n=32) had age of 47±11 years (mean±standard deviation, range, 27–65). Patients (n=22) had age of 58±12years (range, 39–80) and all presented with stage IV cancer. Three patients had breast cancer, one patient had colon cancer, one had pancreatic cancer, and 17 patients had prostate cancer. Metastatic lesion locations (liver, brain, axial, and appendicular skeleton) were consistent with sites to which the primary tumors are known to migrate.

### Radiological Metrics

**Conventional metastatic imaging—**There were 91 detected lesions from the CT (n=19) and/or PET/CT(n=3). The lesions were distributed throughout the body, with most appearing

in the spine, pelvis, and liver. Additional sites and locations included extracranial, the calvarium, and lymphadenopathy. One recurrent lesion was not detected by CT in the prostate. Incidental findings, such as hemangiomas, cysts, and degenerative disease of the spine were not counted as lesions.

**WB-MRI—**The WB-$T_2$WI detected 88 lesions (97% of those detected by CT or PET/CT). The WB-DWI detected 84 lesions (92%) (coronal plane), but, in cases where axial images were acquired, the number of lesions detected by WB-DWI increased to 87 lesions (95%). When combined, the $T_2$ and DWI/ADC mapping resulted in a 96% detection rate. In general, the WB-$T_2$WI provided a global view of anatomical information in one setting. Excellent soft tissue delineation was seen in the thorax and abdomen, with good separation of multiple organs, ribs, sternum, and other tissue in these regions.

The DWI and ADC mapping of the different regions were excellent, except in some circumstances in the neck and thorax in the coronal plane. For example, when using DWI, in the thorax and coronal plane, artifacts degraded the image quality and obscured the anatomy due to cardiac and breathing motion. However, by acquiring DWI in the axial plane, motion-related artifacts decreased and improved normal anatomical and lesion detection was noted (see Figure 2). In addition, by using PACE navigators during the DWI acquisition resulted in improved thoracic scanning in the coronal or sagittal plane (Figures 1 and 3).

Figure 3 demonstrates the ability of WB-DWI to define the extent of metastatic disease in patients, specifically, in the liver, spine, and pelvis. For example, the WB-DWI at b values of b=400s/mm$^2$ and b=800 s/mm$^2$ appear to show different degrees of metastatic disease in the left iliac wing and liver in this patient. Moreover, the ADC map values are significantly different ($p<0.002$) from that of normal and metastatic bone in the same regions. Figure 4 demonstrates the integration of WB-MRI $T_2$WI and DWI with PET/CT imaging to characterize lesion tissue using quantitative radiological biomarkers of SUV and ADC mapping. Similarly, Figure 5 demonstrates WB-DWI with ADC mapping as a potential screening tool, where, coronal WB-ADC mapping was able to detect a recurrence of primary prostate cancer in a patient with rising PSA after radiation treatment. The lesion in the prostate was not detected on CT. Specifically, a region with low ADC map values in the right peripheral zone of the prostate was visualized by the WB-MRI. This observation allowed for “on the fly” high-resolution $T_2$WI, DWI/ADC, and DCE imaging to be performed to confirm recurrent disease.

## Diffusion-Weighted Imaging/ADC Mapping

Whole Body-DWI had a sensitivity of 92% for the detection of metastatic disease using the coronal acquisition of images from various regions of the body. However, the sensitivity increased significantly (95%) if the coronal thoracic regions were excluded from this analysis. In the cases where axial DWI was obtained in the thorax, metastatic disease was clearly visible, as shown in Figure 2.

Figure 3 demonstrates the use of WB-MRI to define the extent and progression of metastatic disease in a 46 year old female patient over a nine-month period during adjuvant therapy. At the baseline scan (data not shown), there was a solitary bony lesion in the left ischium seen

on both PET/CT and WB-MRI. However, the metastatic disease progressed to include the entire left pelvis and multiple sites within the liver and spine (see Figure 4). The use of WB-MRI enabled the acquisition of different anatomical planes for increased diagnostic capabilities and define the extent of disease (see Figures 3–5).

The typical ADC map values for bone in healthy subjects were 0.43±0.18 $\times 10^{-3}$mm$^2$/s (cervical vertebrae), 0.29±0.20 $\times 10^{-3}$mm$^2$/s(thoracic vertebrae), 0.33±0.20 $\times 10^{-3}$mm$^2$/s(lumbar vertebrae), 0.43±0.17 $\times 10^{-3}$mm$^2$/s (iliac crest), and 0.21±0.16 $\times 10^{-3}$mm$^2$/s (femur). For soft tissue, healthy subjects ADC map values for liver were 1.16±0.22 $\times 10^{-3}$mm$^2$/s (right lobes), 1.12±0.26 $\times 10^{-3}$mm$^2$/s (left lobes); for the pancreas (tail), 1.40±0.27 $\times 10^{-3}$mm$^2$/s; for kidneys: (right) 1.93±0.14 $\times 10^{-3}$mm$^2$/s and (left) 1.94±0.11 $\times 10^{-3}$mm$^2$/s; for breast glandular tissue, 1.94 ±0.33 $\times 10^{-3}$mm$^2$/s (right), and 1.91 ±0.27 $\times 10^{-3}$mm$^2$/s (left); and for prostate, peripheral zone (PZ), 1.68±0.17 $\times 10^{-3}$mm$^2$/s (right) and 1.69±0.23 $\times 10^{-3}$mm$^2$/s(left). In patients with metastatic disease, ADC map values for lesions were as follows: 0.82±0.13 $\times 10^{-3}$mm$^2$/s (thoracic vertebrae); 0.99±0.19 $\times 10^{-3}$mm$^2$/s (lumbar), 0.57±0.45 $\times 10^{-3}$mm$^2$/s (iliac crest); and 0.85±0.21 $\times 10^{-3}$mm$^2$/s in liver. These ADC map values were significantly different ($p<0.002$) between the metastatic sites and normal tissue and are summarized in Tables 1 and 2.

### ADC ratios and Standardized Uptake Values in normal and lesion tissue

In the control subjects, the ADC ratio between different tissue types was very similar (0.97±0.04) in most regions. In bone, the Iliac crest (0.96) and femur (0.91) the ADC ratios were lower. In patients with metastatic lesions, interesting, slightly higher normal ADC ratios (1.01±0.06) were noted in soft tissue organ sites. The ADC ratios ranged from (0.74–1.33) in normal appearing bone in tumor patients. But, in bony metastatic sites, the ADC ratios were increased in the thoracic vertebrae (3.04), lumbar vertebrae (3.00), Iliac crest (2.63), femur (5.0), and pelvis (5.29). In metastatic soft tissue lesions demonstrated an opposite trend, the ADC ratios were decreased in the liver (0.79) and prostate (0.69) compared to normal tissues in these organs. Metastatic lesion PET SUV values were 3.2±0.04 (vertebrae), 4.0±0.2 (iliac crest), and 7.0±0.9 in the liver. The reference PET SUV value in the liver was 1.7±0.04.

## Discussion

We have demonstrated the feasibility of using multiparametric quantitative WB-MRI, consisting of $T_2$WI, $T_1$WI, and DWI with ADC mapping at 3T, for detection and characterization of normal and lesion tissue in healthy and cancer patients. The quantitative WB-ADC map values were significantly different between normal tissue and metastatic lesions. Interestingly, normal tissue values of ADC mapping in metastatic patients was different than the same tissue in healthy subjects, suggesting changes within the “normal tissue environment” due to the presence of metastatic lesions. There were significant decreases in the ADC map values in metastatic lesions in soft tissue compared to normal viscera in healthy subjects and patients with concurrent decreases in the ADC ratio between the same tissue. The ADC map values in soft tissue from our WB-MRI are very consistent with those values reported using localized and WB-MRI imaging of different organs

(12,16,32–36). Moreover, our study provides a set of normative ADC values in different tissue and organs from a large group of healthy subjects for quantitative metrics of normal tissue. For example, using literature normative ADC values from the pelvis, the ADC values were between 0.32±0.2 and 0.31±0.1 with the ADC ratio=1.03 (calculated by our method) and for bone marrow the ADC ratios were between 0.57–0.60. (36,37). These results in ADC values from bone lesions from the current study are consistent with the previously published reports. Moreover, the ADC map values and ADC ratio in metastatic bone lesions were increased compared to normal bone tissue, which may suggest a pathological process.

The advantage of using quantitative ADC map values is that ADC provides radiological biomarkers to differentiate between benign and malignant tissue. The introduction of the ADC ratio demonstrates a reproducible metric that could be used in clinical trials to gauge treatment response (18).

The improved WB-MRI provides several attractive features, such as, increased anatomical coverage from the head to the mid-tibia in a clinically feasible time and excellent spatial resolution. The use of continuous table movement allows for acquisition of “seamless” data during scanning using dedicated phased array coils. This allows for the acquisition of multiple anatomical planes within the body and enables WB-MRI to be tailored to fit the patient, such that an “individualized patient sequence” can be developed. Most radiological applications for metastatic disease involve localized MR imaging, which may miss “hidden” or “distant” disease not located in the area of interrogation. There are only a few radiological modalities that can image the entire body and these require radiation or injection of radionuclides for tumor detection. WB-MRI does not require radiation and provides a similar or even superior tissue delineation and coverage than nuclear medicine methods, either PET and/or CT, combined (38–41). In fact, by combining PET/CT with multiparametric WB-MRI methods, important biophysical information can be obtained about both the primary and metastatic tumor environment beyond standard volumetric data, which will lead to a better characterization of the lesion. For example, PET/CT imaging is an effective method for the staging of different cancers using $^{18}$FDG (or other radionuclides) because tumors have increased glucose metabolism (42,43). Similarly, WB-MRI can image tumors with several different sequences that probe the different states of water and provide varying tissue contrasts depending on the MRI parameters. By combining, WB-MRI and PET/CT together provides a basis for improved detection and characterization of tumors which could be used as surrogate biomarkers to monitor the response to treatment or the inadequacy of therapeutic intervention. This is consistent with published reports that employ localized MRI with and/or PET/CT imaging methods (44–47).

There are some limitations to PET, such as, lower spatial resolution than MRI, and the use of radionuclides in multiple settings. Nevertheless, PET/CT is needed and should be complemented with WB-MRI to fully characterize tissue in the body. Moreover, with increasing deployment of PET/MR imaging devices, there is a need to better understand the complementary biophysical information obtained from each distinct modality about different tissue types(48–50).

There are some limitations to the use of WB-DWI, for example, coronal imaging of the neck or thoracic areas. Our experience demonstrated major motion and ghosting artifacts in these regions, with some decreases in these artifacts by using automatic navigator-corrected schemes employed by the scanner. Thus, we recommend that WB-DWI scanning be performed in the axial plane, if metastasis is suspected in the neck or thorax regions. Finally, this is a limited study with a small sample size and larger studies need to be performed to accurately gauge the influence of multiparametric WB-MRI in the clinical setting.

## Conclusions

In summary, we have demonstrated that multiparametric WB-MRI, which includes quantitative ADC mapping identifies normal tissue and metastatic lesions at 3T and established a set of normative ADC map values for normal tissue from healthy subjects. These WB-MRI methods can be used to quantify new metrics and provide the basis for a comprehensive evaluation of tissue assessment for staging and response during treatment.

## Acknowledgments

This work was supported in part by 5P30CA06973 (IRAT), 1R01CA190299, U01CA140204, JHU-2012-MR-86-01-36819 and equipment donation from NVidia.

National Institutes of Health grant numbers: 5P30CA006973 (IRAT), U01CA140204, 1R01CA190299, Siemens Medical Grant:JHU-2012-MR-86-01-36819 and The Tesla K40 GPU card used for this research was donated by the NVIDIA Corporation.

## References

1. Hortobagyi GN. Bone metastases in breast cancer patients. Semin Oncol. 1991; 18(4 Suppl 5):11–15.
2. Lu J, Steeg PS, Price JE, et al. Breast cancer metastasis: challenges and opportunities. Cancer Res. 2009; 69(12):4951–4953. [PubMed: 19470768]
3. Cook GJ, Houston S, Rubens R, Maisey MN, Fogelman I. Detection of bone metastases in breast cancer by 18FDG PET: differing metabolic activity in osteoblastic and osteolytic lesions. Journal of clinical oncology. 1998; 16(10):3375–3379. [PubMed: 9779715]
4. Yang HL, Liu T, Wang XM, Xu Y, Deng SM. Diagnosis of bone metastases: a meta-analysis comparing 18FDG PET, CT, MRI and bone scintigraphy. Eur Radiol. 2011; 21(12):2604–2617. [PubMed: 21887484]
5. Ballon D, Dyke J, Schwartz LH, et al. Bone marrow segmentation in leukemia using diffusion and T (2) weighted echo planar magnetic resonance imaging. NMR Biomed. 2000; 13(6):321–328. [PubMed: 11002312]
6. Daldrup-Link HE, Franzius C, Link TM, et al. Whole-Body MR Imaging for Detection of Bone Metastases in Children and Young Adults: Comparison with Skeletal Scintigraphy and FDG PET. Am J Roentgenol. 2001; 177(1):229–236. [PubMed: 11418435]
7. Hargaden G, O'Connell M, Kavanagh E, et al. Current Concepts in Whole-Body Imaging Using Turbo Short Tau Inversion Recovery MR Imaging. Am J Roentgenol. 2003; 180(1):247–252. [PubMed: 12490514]
8. Johnston C, Brennan S, Ford S, Eustace S. Whole body MR imaging: applications in oncology. Eur J Surg Oncol. 2006; 32(3):239–246. [PubMed: 16427246]
9. Li S, Sun F, Jin ZY, Xue HD, Li ML. Whole-body diffusion-weighted imaging: technical improvement and preliminary results. J Magn Reson Imaging. 2007; 26(4):1139–1144. [PubMed: 17896396]

10. Stecco A, Romano G, Negru M, et al. Whole-body diffusion-weighted magnetic resonance imaging in the staging of oncological patients: comparison with positron emission tomography computed tomography (PET-CT) in a pilot study. Radiol Med. 2008
11. Karpitschka M, Godau-Kellner P, Kellner H, et al. Assessment of therapeutic response in ankylosing spondylitis patients undergoing anti-tumour necrosis factor therapy by whole-body magnetic resonance imaging. Eur Radiol. 2013; 23(7):1773–1784. [PubMed: 23494493]
12. Blackledge MD, Collins DJ, Tunariu N, et al. Assessment of treatment response by total tumor volume and global apparent diffusion coefficient using diffusion-weighted MRI in patients with metastatic bone disease: a feasibility study. PloS one. 2014; 9(4):e91779. [PubMed: 24710083]
13. Chhabra A, Carrino JA, Farahani SJ, et al. Whole-body MR neurography: Prospective feasibility study in polyneuropathy and Charcot-Marie-Tooth disease. J Magn Reson Imaging. 2016; 44(6): 1513–1521. [PubMed: 27126998]
14. Axelsen MB, Eshed I, Ostergaard M, et al. Monitoring total-body inflammation and damage in joints and entheses: the first follow-up study of whole-body magnetic resonance imaging in rheumatoid arthritis. Scandinavian journal of rheumatology. 2017; 46(4):253–262. [PubMed: 28125360]
15. Chenevert TL, Stegman LD, Taylor JM, et al. Diffusion magnetic resonance imaging: an early surrogate marker of therapeutic efficacy in brain tumors. J Natl Cancer Inst. 2000; 92(24):2029–2036. [PubMed: 11121466]
16. deSouza NM, Riches SF, Vanas NJ, et al. Diffusion-weighted magnetic resonance imaging: a potential non-invasive marker of tumour aggressiveness in localized prostate cancer. Clin Radiol. 2008; 63(7):774–782. [PubMed: 18555035]
17. Padhani AR, Liu G, Mu-Koh D, et al. Diffusion-weighted magnetic resonance imaging as a cancer biomarker: consensus and recommendations. Neoplasia. 2009; 11(2):102–125. [PubMed: 19186405]
18. Ei Khouli RH, Jacobs MA, Mezban SD, et al. Diffusion-weighted imaging improves the diagnostic accuracy of conventional 3.0-T breast MR imaging. Radiology. 2010; 256(1):64–73. [PubMed: 20574085]
19. Takahara T, Imai Y, Yamashita T, et al. Diffusion weighted whole body imaging with background body signal suppression (DWIBS): technical improvement using free breathing, STIR and high resolution 3D display. Radiat Med. 2004; 22(4):275–282. [PubMed: 15468951]
20. Koh DM, Takahara T, Imai Y, Collins DJ. Practical aspects of assessing tumors using clinical diffusion-weighted imaging in the body. Magn Reson Med Sci. 2007; 6(4):211–224. [PubMed: 18239358]
21. Ohno Y, Koyama H, Onishi Y, et al. Non-small cell lung cancer: whole-body MR examination for M-stage assessment--utility for whole-body diffusion-weighted imaging compared with integrated FDG PET/CT. Radiology. 2008; 248(2):643–654. [PubMed: 18539889]
22. Vilanova JC, Barcelo J. Diffusion-weighted whole-body MR screening. European journal of radiology. 2008; 67(3):440–447. [PubMed: 18430538]
23. Heusner TA, Kuemmel S, Koeninger A, et al. Diagnostic value of diffusion-weighted magnetic resonance imaging (DWI) compared to FDG PET/CT for whole-body breast cancer staging. Eur J Nucl Med Mol Imaging. 2010; 37(6):1077–1086. [PubMed: 20204355]
24. Lin C, Itti E, Luciani A, et al. Whole-body diffusion-weighted imaging with apparent diffusion coefficient mapping for treatment response assessment in patients with diffuse large B-cell lymphoma: pilot study. Invest Radiol. 2011; 46(5):341–349. [PubMed: 21263330]
25. Schmidt GP, Baur-Melnyk A, Haug A, et al. Comprehensive imaging of tumor recurrence in breast cancer patients using whole-body MRI at 1.5 and 3 T compared to FDG-PET-CT. European journal of radiology. 2008; 65(1):47–58. [PubMed: 18082989]
26. Fayad LM, Blakeley J, Plotkin S, Widemann B, Jacobs MA. Whole Body MRI at 3T with Quantitative Diffusion Weighted Imaging and Contrast-Enhanced Sequences for the Characterization of Peripheral Lesions in Patients with Neurofibromatosis Type 2 and Schwannomatosis. ISRN Radiology. 2013; 2013:9.

27. Ahlawat S, Baig A, Blakeley JO, Jacobs MA, Fayad LM. Multiparametric whole-body anatomic, functional, and metabolic imaging characteristics of peripheral lesions in patients with schwannomatosis. J Magn Reson Imaging. 2016; 44(4):794–803. [PubMed: 26991037]
28. Schweitzer ME, Levine C, Mitchell DG, Gannon FH, Gomella LG. Bull's-eyes and halos: useful MR discriminators of osseous metastases. Radiology. 1993; 188(1):249–252. [PubMed: 8511306]
29. Mirowitz SA, Apicella P, Reinus WR, Hammerman AM. MR imaging of bone marrow lesions: relative conspicuousness on T1-weighted, fat-suppressed T2-weighted, and STIR images. Am J Roentgenol. 1994; 162(1):215–221. [PubMed: 8273669]
30. Thie JA. Understanding the Standardized Uptake Value, Its Methods, and Implications for Usage. J Nucl Med. 2004; 45(9):1431–1434. [PubMed: 15347707]
31. Wahl RL, Jacene H, Kasamon Y, Lodge MA. From RECIST to PERCIST: Evolving Considerations for PET response criteria in solid tumors. J Nucl Med. 2009; 50(Suppl 1):122S–150S. [PubMed: 19403881]
32. Yoshikawa T, Kawamitsu H, Mitchell DG, et al. ADC measurement of abdominal organs and lesions using parallel imaging technique. Am J Roentgenol. 2006; 187(6):1521–1530. [PubMed: 17114546]
33. Yuan Z, Ye XD, Dong S, et al. Role of magnetic resonance diffusion-weighted imaging in evaluating response after chemoembolization of hepatocellular carcinoma. European journal of radiology. 2010; 75(1):e9–14.
34. Eiber M, Holzapfel K, Ganter C, et al. Whole-body MRI including diffusion-weighted imaging (DWI) for patients with recurring prostate cancer: technical feasibility and assessment of lesion conspicuity in DWI. J Magn Reson Imaging. 2011; 33(5):1160–1170. [PubMed: 21509875]
35. Vermathen P, Binser T, Boesch C, Eisenberger U, Thoeny HC. Three-year follow-up of human transplanted kidneys by diffusion-weighted MRI and blood oxygenation level-dependent imaging. J Magn Reson Imaging. 2012; 35(5):1133–1138. [PubMed: 22180302]
36. Lavdas I, Rockall AG, Castelli F, et al. Apparent Diffusion Coefficient of Normal Abdominal Organs and Bone Marrow From Whole-Body DWI at 1.5 T: The Effect of Sex and Age. Am J Roentgenol. 2015; 205(2):242–250. [PubMed: 26204271]
37. Oner AY, Aggunlu L, Akpek S, Tali T, Celik A. Diffusion-weighted imaging of the appendicular skeleton with a non-Carr-Purcell-Meiboom-Gill single-shot fast spin-echo sequence. Am J Roentgenol. 2007; 189(6):1494–1501. [PubMed: 18029891]
38. Yang HL, Liu T, Wang XM, Xu Y, Deng SM. Diagnosis of bone metastases: a meta-analysis comparing (1)(8)FDG PET, CT, MRI and bone scintigraphy. Eur Radiol. 2011; 21(12):2604–2617. [PubMed: 21887484]
39. Lecouvet FE, El Mouedden J, Collette L, et al. Can whole-body magnetic resonance imaging with diffusion-weighted imaging replace Tc 99m bone scanning and computed tomography for single-step detection of metastases in patients with high-risk prostate cancer? European urology. 2012; 62(1):68–75. [PubMed: 22366187]
40. Shen G, Deng H, Hu S, Jia Z. Comparison of choline-PET/CT, MRI, SPECT, and bone scintigraphy in the diagnosis of bone metastases in patients with prostate cancer: a meta-analysis. Skeletal radiology. 2014; 43(11):1503–1513. [PubMed: 24841276]
41. Pasoglou V, Michoux N, Peeters F, et al. Whole-body 3D T1-weighted MR imaging in patients with prostate cancer: feasibility and evaluation in screening for metastatic disease. Radiology. 2015; 275(1):155–166. [PubMed: 25513855]
42. Wahl RL. Positron Emission Tomography (PET): an update on applications in breast cancer. Breast Dis. 1998; 10(3–4):165–175. [PubMed: 15687572]
43. Reske SN, Blumstein NM, Neumaier B, et al. Imaging prostate cancer with 11C-choline PET/CT. J Nucl Med. 2006; 47(8):1249–1254. [PubMed: 16883001]
44. Chen X, Moore MO, Lehman CD, et al. Combined use of MRI and PET to monitor response and assess residual disease for locally advanced breast cancer treated with neoadjuvant chemotherapy. Acad Radiol. 2004; 11(10):1115–1124. [PubMed: 15530804]
45. Judenhofer MS, Wehrl HF, Newport DF, et al. Simultaneous PET-MRI: a new approach for functional and morphological imaging. Nat Med. 2008; 14(4):459–465. [PubMed: 18376410]

46. Uematsu T, Kasami M, Yuen S. Comparison of FDG PET and MRI for evaluating the tumor extent of breast cancer and the impact of FDG PET on the systemic staging and prognosis of patients who are candidates for breast-conserving therapy. Breast Cancer. 2009; 16(2):97–104. [PubMed: 18663562]

47. Jacobs MA, Wolff A, Ouwerkerk R, et al. Monitoring of neoadjuvant chemotherapy using multiparametric, (23)Na sodium MR, and multimodality (PET/CT/MRI) imaging in locally advanced breast cancer. Breast Cancer Res Treat. 2011; 128(1):119–126. [PubMed: 21455671]

48. Antoch G, Bockisch A. Combined PET/MRI: a new dimension in whole-body oncology imaging? Eur J Nucl Med Mol Imaging. 2009; 36(Suppl 1):S113–120. [PubMed: 19104802]

49. Buchbender C, Heusner TA, Lauenstein TC, Bockisch A, Antoch G. Oncologic PET/MRI, part 1: tumors of the brain, head and neck, chest, abdomen, and pelvis. J Nucl Med. 2012; 53(6):928–938. [PubMed: 22582048]

50. Buchbender C, Heusner TA, Lauenstein TC, Bockisch A, Antoch G. Oncologic PET/MRI, part 2: bone tumors, soft-tissue tumors, melanoma, and lymphoma. J Nucl Med. 2012; 53(8):1244–1252. [PubMed: 22782313]

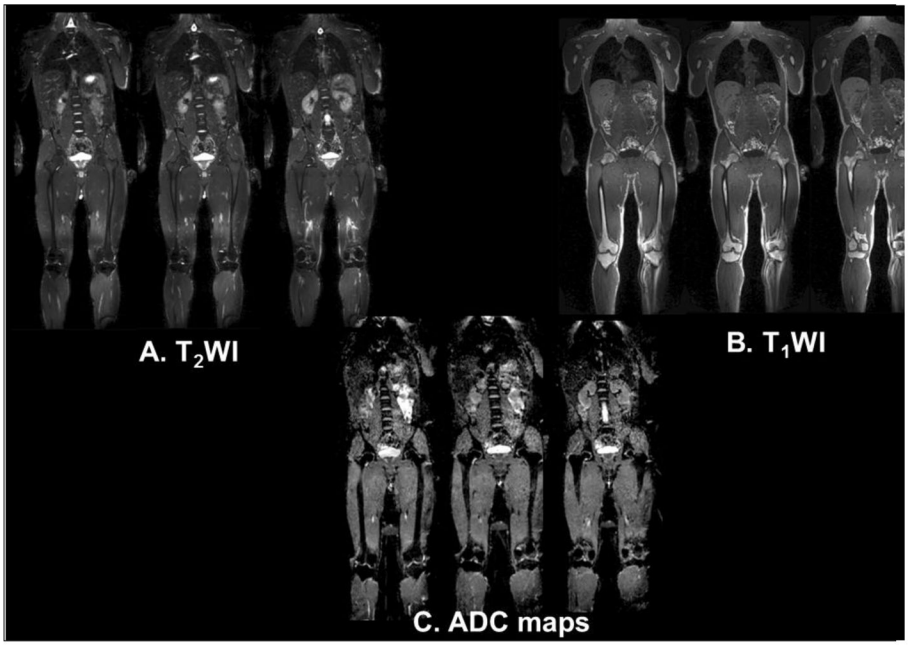


**Figure 1.**

Demonstration of multiparametric whole-body MRI in a normal subject. **A**. T2-weighted imaging through the central slices in the body. **B.** T1-weighted images and **C**. ADC maps of the same location in the normal subject.

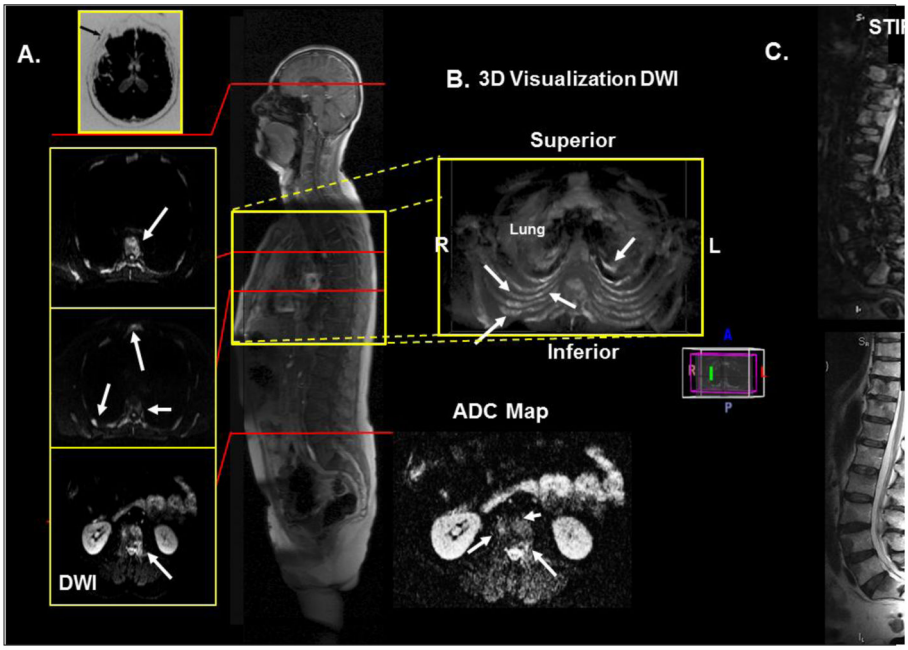


**Figure 2.**

Demonstration of WB-MRI on a 66-year-old man with metastatic prostate cancer. **A**. Axial diffusion imaging through the thorax and pelvis shows multiple metastatic lesions in the ribs, sternum, and vertebrae. **B.** 3D visualization of the thorax showing the metastatic lesions in the chest. **C.** T2 and STIR imaging of the spine to correlate the metastatic lesions with the WB-MRI.

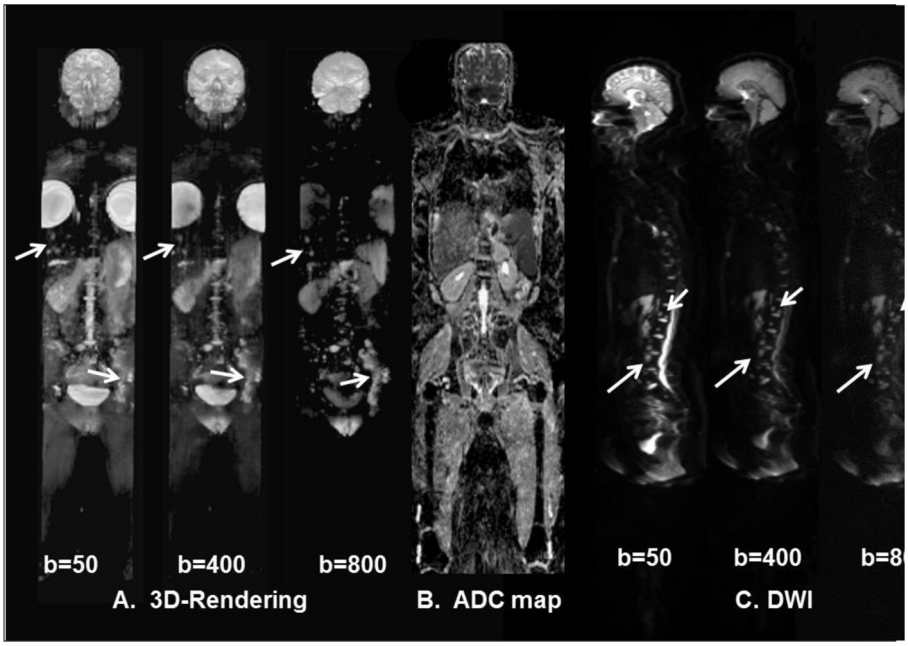


**Figure 3.**

Demonstration of the of the WB-DWI in a 46-year-old- woman with metastatic breast cancer. **A.)** Three-dimensional visualization of metastatic lesions using different b values from the DWI. There are progressive changes in the DWI signal intensity within the metastatic sites (white arrows) of the left pelvis, thoracic and lumbar spine, and liver. **B.)** A coronal ADC map through the midsection of the patient. **C.)** Different b-values from WB-DWI sagittal images of the spine showing multiple metastatic regions.

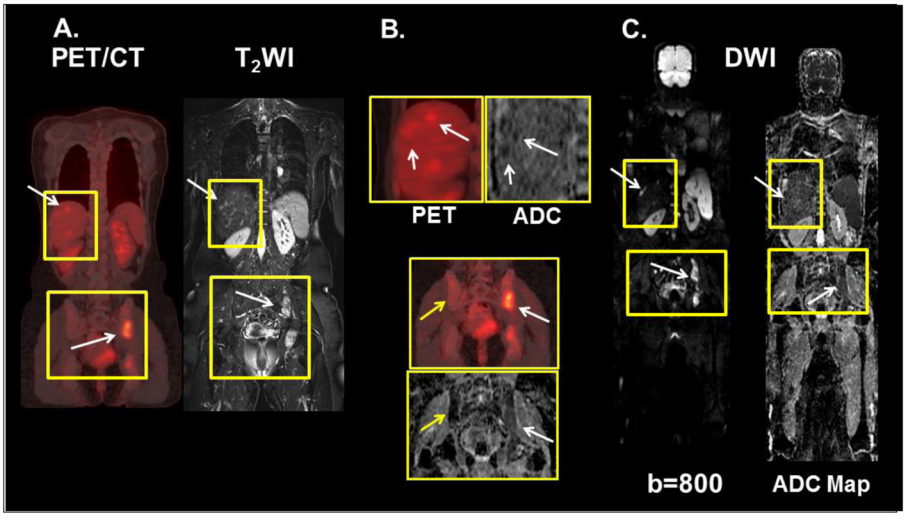


**Figure 4.**

Demonstration of the WB-MRI and PET/CT in a 46-year-old woman with metastatic breast cancer in the liver and pelvis. **A.**) The white arrows in liver and pelvis show metastatic lesions on PET and T2-weighted images. **B.**) The PET and ADC maps demonstrate the metastatic lesions (white arrows) in the liver. In the pelvis, the yellow arrows indicate normal bone on the ADC map and PET. The white arrows show the metastatic lesions. **C.**) The same metastatic sites are noted on the WB-MRI diffusion-weighted images (b=800) and the ADC map.

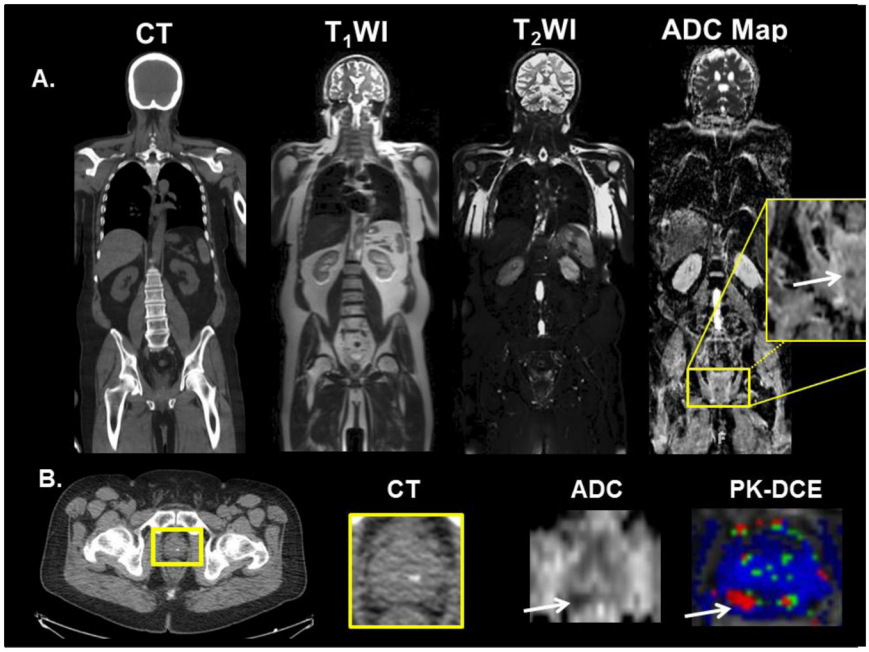


**Figure 5.**

Example of WB-MRI screening in 60-year-old man with a stage T2B, Gleason 9 with increasing PSA, post external beam radiation and androgen deprivation therapy. **A.** CT and whole-body MRI was performed for interrogation of metastatic disease. Potential recurrence was only found in the right peripheral zone on the WB-ADC map and shown in the yellow box. **B**. Localized MRI with DWI/ADC and Pharmacokinetic-DCE (PK-DCE) was performed "*on the fly*" for confirmation of prostate cancer recurrence.

**Table 1a**

Regional ADC map values from healthy subjects

| Normals (n=32) | ADC $10^{-3}mm^2/s$ | | ADC $10^{-3}mm^2/s$ | | |
|---|---|---|---|---|---|
| **Tissue** | **Normal (Rt)** | **S.D. (±)** | **Normal (Lt)** | **S.D. (±)** | **ADC Ratio** |
| Cerebral Cortex | 0.83 | 0.14 | 0.83 | 0.06 | 1.00 |
| Cerebellum | 0.68 | 0.06 | 0.70 | 0.06 | 0.97 |
| Lateral Ventricle | 3.01 | 0.41 | 3.14 | 0.19 | 0.96 |
| Breast Glandular | 1.94 | 0.33 | 1.91 | 0.27 | 1.02 |
| Gall bladder | 2.85 | 0.28 | | | |
| Liver | 1.16 | 0.22 | 1.12 | 0.26 | 1.04 |
| Spleen | 0.79 | 0.07 | | | |
| Pancreas(Tail) | 1.40 | 0.19 | | | |
| Kidney | 1.93 | 0.14 | 1.94 | 0.11 | 0.99 |
| Prostate (PZ) | 1.68 | 0.17 | 1.69 | 0.23 | 0.99 |
| Iliac crest | 0.43 | 0.17 | 0.45 | 0.18 | 0.96 |
| Femur | 0.21 | 0.16 | 0.23 | 0.15 | 0.91 |
| Pelvis | 0.43 | 0.13 | 0.48 | 0.18 | 0.90 |
| Psoas muscle | 1.35 | 0.23 | 1.34 | 0.20 | 1.01 |
| Urinary bladder | 3.20 | 0.21 | | | |
| Uterus | 1.27 | 0.20 | | | |
| Vertebral disk | 1.59 | 0.19 | | | |
| Vertebral bone (Cervical) | 0.43 | 0.18 | | | |
| Vertebral bone (Thoracic) | 0.29 | 0.20 | | | |
| Vertebral bone (Lumbar) | 0.33 | 0.20 | | | |

ADC=Apparent Diffusion Coefficient, Rt=Right, Lt=Left, SD=Standard Deviation, PZ=peripheral zone

ADC Ratio = contralateral tissue divided by ipsilateral tissue ADC map values

**Table 1b**

Regional normal ADC map values from patients

| Patients (n=22) | ADC $10^{-3}mm^2/s$ | | ADC $10^{-3}mm^2/s$ | | |
|---|---|---|---|---|---|
| **Tissue** | **Normal (Rt)** | **S.D. (±)** | **Normal (Lt)** | **S.D. (±)** | **ADC Ratio** |
| Cerebral Cortex | 0.82 | 0.08 | 0.84 | 0.14 | 0.98 |
| Cerebellum | 0.67 | 0.12 | 0.66 | 0.12 | 1.02 |
| Lateral Ventricle | 3.30 | 0.24 | 3.23 | 0.22 | 1.02 |
| Breast Glandular | 1.85 | 0.58 | 1.61 | 0.08 | 1.15 |
| Gall bladder | 2.75 | 0.20 | | | |
| Liver | 0.99 | 0.24 | 1.01 | 0.22 | 0.98 |
| Spleen | 0.78 | 0.11 | | | |
| Pancreas(Tail) | 1.54 | 0.24 | | | |
| Kidney | 1.85 | 0.17 | 1.85 | 0.13 | 1.00 |
| Prostate (PZ) | 1.45 | 0.15 | 1.42 | 0.10 | 1.02 |
| Iliac crest | 0.31 | 0.19 | 0.32 | 0.20 | 0.97 |
| Femur | 0.17 | 0.15 | 0.23 | 0.17 | 0.74 |
| Pelvis | 0.32 | 0.14 | 0.24 | 0.26 | 1.33 |
| Psoas muscle | 1.19 | 0.27 | 1.32 | 0.19 | 0.90 |
| Urinary bladder | 2.90 | 0.24 | | | |
| Uterus | 1.42 | 0.13 | | | |
| Vertebral disk | 1.53 | 0.16 | | | |
| Vertebral bone (Cervical) | 0.60 | 0.17 | | | |
| Vertebral bone (Thoracic) | 0.27 | 0.18 | | | |
| Vertebral bone (Lumbar) | 0.33 | 0.21 | | | |

ADC=Apparent Diffusion Coefficient, Rt=Right, Lt=Left, S.D.=Standard Deviation, PZ= peripheral zone

Ratio = contralateral tissue divided by ipsilateral tissue ADC map values

*Acad Radiol*. Author manuscript; available in PMC 2019 November 01.

**Table 1c**

ADC map values from metastatic lesions in patients

| Metastatic Lesions | ADC $10^{-3}mm^2/s$ | | ADC $10^{-}mm^2/s$ | | |
|---|---|---|---|---|---|
| **Tissue** | **Lesion** | **S.D. (±)** | **Normal** | **S.D. (±)** | **Ratio** |
| Vertebral bone (Thoracic) | 0.82 | 0.13 | 0.27 | 0.18 | 3.04 |
| Vertebral bone (Lumbar) | 0.99 | 0.19 | 0.33 | 0.21 | 3.00 |
| Pelvis | 0.90 | 0.10 | 0.17 | 0.15 | 5.29 |
| Femur | 1.60 | 0.23 | 0.32 | 0.14 | 5.00 |
| Iliac crest | 0.84 | 0.45 | 0.32 | 0.07 | 2.63 |
| Liver | 0.88 | 0.27 | 1.12 | 0.26 | 0.79 |
| Prostate (PZ) | 1.00 | 0.07 | 1.45 | 0.15 | 0.69 |

ADC=Apparent Diffusion Coefficient, Rt=Right, Lt=Left, SD=Standard Deviation, PZ=peripheral zone

Ratio = Lesion tissue divided by normal tissue ADC

**Table 2**

ADC map values from metastatic lesions in patients

| Metastatic Lesions | ADC $10^{-3}mm^2/s$ | | ADC $10^{-}mm^2/s$ | | |
|---|---|---|---|---|---|
| **Tissue** | **Lesion** | **S.D. (±)** | **Normal** | **S.D. (±)** | **Ratio** |
| Vertebral bone (Thoracic) | 0.82 | 0.13 | 0.27 | 0.18 | 3.04 |
| Vertebral bone (Lumbar) | 0.99 | 0.19 | 0.33 | 0.21 | 3.00 |
| Pelvis | 0.90 | 0.10 | 0.17 | 0.15 | 5.29 |
| Femur | 1.60 | 0.23 | 0.32 | 0.14 | 5.00 |
| Iliac crest | 0.84 | 0.45 | 0.32 | 0.07 | 2.63 |
| Liver | 0.88 | 0.27 | 1.12 | 0.26 | 0.79 |
| Prostate (PZ) | 1.00 | 0.07 | 1.45 | 0.15 | 0.69 |

ADC=Apparent Diffusion Coefficient, Rt=Right, Lt=Left, SD=Standard Deviation, PZ=peripheral zone

Ratio = Lesion tissue divided by normal tissue ADC